

# Design of a Reflective Intensity Optical Fibre Bundle Displacement Sensor

Binghui Jia<sup>\*</sup>, Jing Yu, Yong Feng, Min Zhang and Gang Li

(School of Mechanical Engineering, Nanjing Institute of Technology, Nanjing 211167, China)

**Abstract:** Optical fibre sensor has the advantages of small size, light weight, anti-electromagnetic interference, and high measurement accuracy, which has important applications in research and industrial production. To design an optical fibre displacement sensor (OFBDS) with simple structure and high measurement accuracy, the unified model of the commonly used OFBDS structures was proposed and the feasibility of the intensity-modulation of multi-structural optical fibre bundles was analysed based on the arrangement characteristics of the fibre bundle end-face. The intensity-modulation characteristic of different fibre bundles was analysed, and the single coil coaxial fibre bundle was chosen as the fibre probe in this study. The sensor hardware system was designed. Lastly, the calibration experiment, temperature interference experiment, changes of measured plane surface area, and the dynamic experiment were conducted. Results showed that the sensor linear measurement range was about 3 mm, and the sensor system had excellent static and dynamic characteristics.

**Keywords:** optical fibre bundle displacement sensor; intensity-modulation characteristic; static experiment; dynamic experiment

**CLC number:** TH7

**Document code:** A

## 1 Introduction

Optical fibre displacement measurement technology is an important part of optical fibre sensing technology, which has been applied in all kinds of non-contact measurement because it has high precision, high adaptability, corrosion resistance, high temperature resistance, and is immune to electromagnetic interference. At present, there are two main methods for realizing optical fibre displacement detection. One uses the laser as the coherent light source, and the interferometry is applied to realize the detection of the small displacement. Although the accuracy is very high, the whole system is complex and expensive. The other one is the reflective intensity-modulation technique. The displacement is realized by measuring the light strength reflected from the reflector

through the optical fibres. This approach has the advantages of simple structure, good stability, high accuracy, and low cost, so it has a good prospect in the displacement detection technology and has been studied by scholars all over the world<sup>[1-4]</sup>. Although its measuring principle is intuitionistic, it is essential to build the mathematic models of optical fibre bundle displacement sensors (OFBDS) based on the reflective intensity-modulation technique. It relates to light intensity spatial distribution, the arrangement of optical fibres, the numerical aperture (NA), the fibre core-radius and so on, and usually change of a single parameter can have a huge impact on the OFBDS preference. It is of great significance to carry out research on the modelling analysis of the OFBDS.

Researchers in Refs. [5-6] used the pure Gaussian distribution to calculate the light intensity spatial

Received 2018-11-09.

Sponsored by the National Natural Science Foundation of China (Grant No.51775260), the Qinglan Project of Jiangsu Province (2017) of China and the Funds of Nanjing Institute of Technology (Grant No. CKJA201801).

\*Corresponding author. E-mail: bhjia@njit.edu.cn.

distribution of the transmitting fibre, which was obviously not in line with reality. Jia et al.<sup>[7]</sup> considered that the received light intensity of the receiving fibre could use the light intensity of the transmitting fibre middle point in the virtual fibre front-end as they thought the transmitting fibre radius was very small. However, this inevitably resulted in big calculation errors of the received light intensity, and brought inaccuracy to the research on the modelling of optical fibre bundles with large numbers of fibres. Marzban et al.<sup>[8]</sup> and Xie et al.<sup>[9]</sup> designed specific OFBDS based on their research objects, and the corresponding models were carried out, but they did not propose a method for modelling multi-structure optical fibre bundles.

In this paper, a unified mathematical model is established based on the analysis of five kinds of most studied OFBDS, as shown in Fig.1, including the common structures of dual (D) type, concentric transmitting inside (CTI) type, double circular (DC) type, random (R) type, and hemispherical (H) type, and are matched with the light intensity-modulation characteristics of the pair (P) type. Based on the comparison and analysis of the intensity-modulation characteristic of the abovementioned fibre bundle structure, the optimal fibre bundle structure is selected for displacement sensor design.

## 2 Theoretical Basis of Modelling Multi-structure OFBDS

### 2.1 Most Studied Structures of the OFBDS

At present, there are many different structures of the OFBDS, which have various arrangements of the transmitting fibres (TF) and the receiving fibres (RF). The most adopted are the pair (P) type with a TF and an RF, the dual (D) type with a TF bundle and an RF bundle, the concentric (C) type with a TF (bundle) and a single loop or multiple loops RF around, the random (R) type with a certain amount of randomly arranged TF and RF, and the hemispherical (H) type with half TF and half RF.

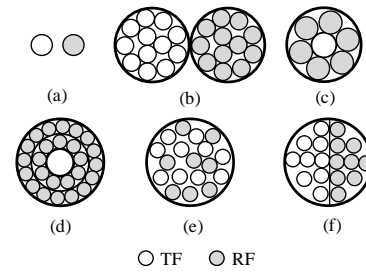


**Fig.1 Cross-sectional front-end view of the common types of the OFBDS: (a) P type; (b) D type; (c) CTI type; (d) DC type; (e) R type; (f) H type**

Each type of the OFBDS can be regarded as a combination of one or more P type OFBDS in the structure. Each type has different arrangement of optical fibres in the front-end, thus the light intensity coupled to RF from TF is not alike and it causes great difference in the modulation characteristics of each type.

### 2.2 Working Principle of the OFBDS

The working principle of the OFBDS is shown in Fig.2, where the light emits from the TF in a conical shape and the maximum divergence angle depends on the NA. After the light is reflected by the object surface, some or all light is received by the RF. When the distance between the measurement surface and the OFBDS front-end is changing, the intensity of the reflected light received by RF will change accordingly. Provided that other conditions are invariant, the modulated signal received by the photodetector D is determined by the distance between the measurement surface and the OFBDS front-end. The function of displacement measurement is realized by the detection of the changing modulated signal.

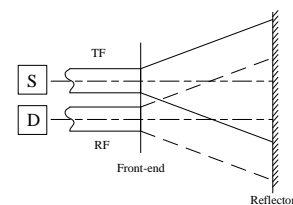


**Fig.2 Working principle of the OFBDS**

### 2.3 Characteristics of Light Intensity Spatial Distribution in Optical Output Field

According to the mode theory of optical fibre transmission, most light power is concentrated near the base and low order modes in a steady state. The radial distribution of the combined light intensity in the optical output field can be approximated by the Gaussian function, which is called Approximate-Gaussian distribution<sup>[10]</sup>. Furthermore, the light that transmits along the fibres can be approximated as plane wave, which is nearly equivalent to the circular hole diffraction formed by the plane wave in the optical output field emitted perpendicularly to the circular hole surface in an opaque screen. As a result, the actual situation is closed to a certain mixture of the above two situations.

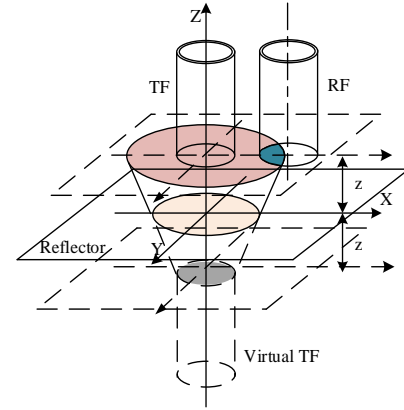
For large core-radius multimode fibres, Yuan<sup>[10]</sup> provided the expression of light intensity spatial distribution in optical output field in Cartesian coordinates as follows:

$$I(x,y,z) = \frac{I_0}{a_0^2 \left[ 1 + \zeta \left( \frac{z}{a_0} \right)^3 \cdot \tan \theta \right]^2} \cdot \exp \left\{ - \frac{x^2 + y^2}{a_0^2 \left[ 1 + \zeta \left( \frac{z}{a_0} \right)^3 \cdot \tan \theta \right]^2} \right\} \quad (1)$$

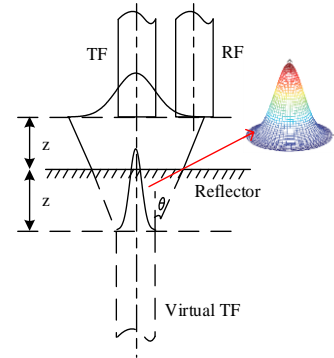
where  $I_0$  (cd) is the maximum received light intensity in the front-end;  $z$  (mm) is the distance between the front-end and the reflector;  $I(x,y,z)$  (lm) is the light flux density of the position  $(x,y,z)$  in the optical output field;  $\sigma$  is the associated parameter which indicates the distribution of fibre refractive index, and  $\sigma=1$  for the step-index fibre;  $a_0$  (mm) denotes the fibre core-radius;  $\zeta$  is the modulation coefficient related to the light source type and the coupling between source and fibre, which indicates the influence of light source property and coupling condition on the intensity distribution in the optical output field; and  $\theta$  (rad) is the maximum divergence angle of the optical fibre.

## 2.4 Intensity-Modulation Function of the P Type OFBDS

For the P type, according to the intensity-modulation function in Eq. (2), it can be calculated by the ratio of light intensity that TF emits and the light intensity that RF receives. The light flux received by the RF equals to that received by the RF from the TF image multiplied by the reflection coefficient of the reflector. The Cartesian coordinates were established based on Fig.3(a).



(a) The cartesian coordinates of the P type



(b) The profiles of light intensity distribution at fiber ends

### Fig.3 Working principle of the P type OFBDS

The intensity-modulation function of the P type OFBDS at the distance  $z$  between the front-end and the reflector is expressed in Eq. (2) as

$$M = \delta \cdot \frac{\iint_{S_r} I(x_r, y_r, z) \cdot S_r ds}{\iint_{S_t} I(x_t, y_t, z) \cdot S_t ds} \quad (2)$$

where  $S_r$  denotes the effective receiving area of the RF;  $S_t$  is the facula area reflected from the reflector in OFBDS front-end surface; and  $\delta$  is the reflection coefficient of the reflector. For the convenience of the subsequent calculation, the reflector was selected as a smooth mirror, thus  $\delta \approx 1$ . For the P type with different parameters, when the distance  $z$  changes, there are

three conditions for the calculation of  $S_r$  as follows: 1) The RF cannot receive any reflected light, and  $S_r=0$ ; 2) Partial RF can receive the reflected light, and  $S_r$  is dynamically changed with the change of  $z$ ; and 3) The RF receives the reflected light completely, and  $S_r$  equals to the area of the RF.

Set the core-radius of TF as  $a_1$ , the maximum divergence angle as  $\theta$  which matches with NA, the axles distance between TF and RF as  $p$ , the distance between the reflector and TF as  $z$ , and the radius of the facula area reflected from the reflector in OFBDS front-end surface as  $q$ , thus  $q=2z\tan\theta+a_1$ . Obviously,  $q$  is changed dynamically with  $z$ , and they have the same

$$M = \frac{\iint_{S_r} I(x_r, y_r, z) \cdot S_r ds}{\iint_{S_t} I(x_t, y_t, z) \cdot S_t ds} = \frac{2 \left( \iint_{S_{ADC}} I(x, y, z) dx dy + \iint_{S_{DCB}} I(x, y, z) dx dy \right)}{4 \iint_{S_{EOB}} I(x, y, z) dx dy} = \frac{\int_0^{\sqrt{a_2^2 - (x-p)^2}} \int_{p-a_2}^{\frac{p^2+q^2-a_2^2}{2p}} I(x, y, z) dx dy + \int_0^{\sqrt{q^2 - x^2}} \int_{\frac{p^2+q^2-a_2^2}{2p}}^q I(x, y, z) dx dy}{2 \int_0^{\sqrt{q^2 - x^2}} \int_0^q I(x, y, z) dx dy} \quad (4)$$

3)  $q > p+a_2$ , that is,  $z > (p+a_2-a_1)/2\tan\theta$ .

In this situation, the RF can completely receive the light reflected from the reflector, and  $S_r$  reaches the maximum, as shown in Fig.4(c).

$$M = \frac{\iint_{S_r} I(x_r, y_r, z) \cdot S_r ds}{\iint_{S_t} I(x_t, y_t, z) \cdot S_t ds} = \frac{\iint_{S_r} I(x_r, y_r, z) \cdot S_r ds}{4 \iint_{S_{FOG}} I(x, y, z) dx dy} = \frac{\int_0^{\sqrt{a_2^2 - (x-p)^2}} \int_{p-a_2}^{p+a_2} I(x, y, z) dx dy}{2 \int_0^{\sqrt{q^2 - x^2}} \int_0^q I(x, y, z) dx dy} \quad (5)$$

variation tendency. Hence, the situations can be discussed according to the change of  $q$ .

1)  $q \leq p-a_2$ , that is,  $z \leq (p-a_2-a_1)/2\tan\theta$ ;

In this situation,  $S_r=0$ , and the received light flux  $\Phi_r=0$ , then

$$M = \frac{\iint_{S_r} I(x_r, y_r, z) \cdot S_r ds}{\iint_{S_t} I(x_t, y_t, z) \cdot S_t ds} = 0 \quad (3)$$

2)  $p-a_2 < q \leq p+a_2$ , that is,  $(p-a_2-a_1)/2\tan\theta < z \leq (p+a_2-a_1)/2\tan\theta$ ;

As shown in Fig.4(b), with the increase of  $z$ ,  $q$  keeps increasing with  $S_r$ .

In conclusion, according to the P type OFBDS working principle and under the assumption that the reflector was regarded as a smooth mirror, the intensity-modulation function of the P type was obtained based on the geometric relationship between the virtual optical output field and the received light area of RF.

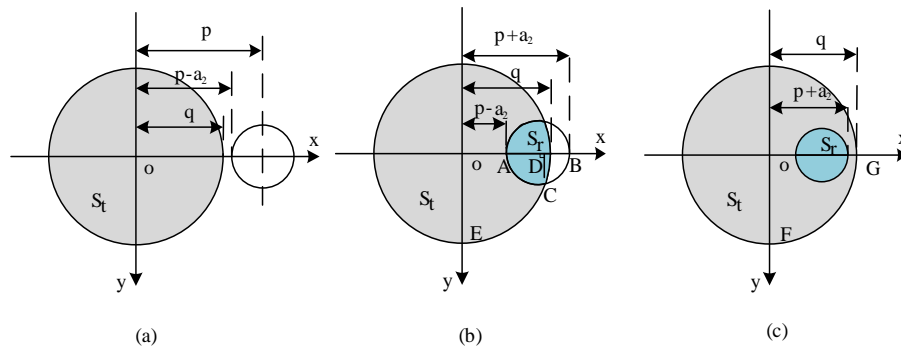


Fig.4 Changes of conditions of  $S_r$

### 3 Modelling of Multi-Structure OFBDS

#### 3.1 D Type

The structure of the D type is shown in Fig.2(b). The TF bundle and the RF bundle are constituted by a certain amount of smaller core-radius fibres, whose radii are  $R_1$  and  $R_2$  respectively and the thickness of

protection are  $p_1$  and  $p_2$ . Assume that all the fibres have the same NA (the same NA makes sure that all the fibres have the same maximum divergence angle), and the two bundles are closely combined, so the axis distance  $p_D = R_1 + p_1 + R_2 + p_2$ . With the aid of Eq. (6), the intensity-modulation function of the D type OFBDS is expressed as follows:

$$M_p = (a_1, a_2, \theta, p, z) = \begin{cases} 0, & z \leq \frac{p - a_2 - a_1}{2 \tan \theta} \\ \frac{\int_0^{\sqrt{a_2^2 - (x-p)^2}} \frac{(p^2 + q^2 - a_2^2)}{2p} I_{(x,y,z)} dx dy + \int_0^{\sqrt{q^2 - x^2}} \frac{\int_{p^2 + q^2 - a_2^2}^q I_{(x,y,z)} dx dy}{2p}}{2 \int_0^{\sqrt{q^2 - x^2}} \int_0^q I_{(x,y,z)} dx dy}, & \frac{p - a_2 - a_1}{2 \tan \theta} < z \leq \frac{p + a_2 - a_1}{2 \tan \theta} \\ \frac{\int_0^{\sqrt{a_2^2 - (x-p)^2}} \int_{p-a_2}^{p+a_2} I_{(x,y,z)} dx dy}{2 \int_0^{\sqrt{q^2 - x^2}} \int_0^q I_{(x,y,z)} dx dy}, & z > \frac{p + a_2 - a_1}{2 \tan \theta} \end{cases}, \quad (6)$$

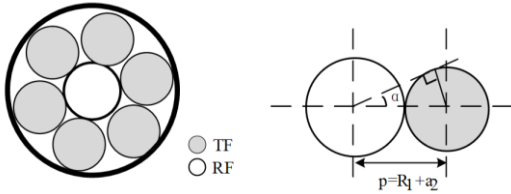
$$M_D(R_1, R_2, \theta, p_D, z) = M(R_1, R_2, \theta, R_1 + p_1 + R_2 + p_2, z) =$$

$$\begin{cases} 0, & z \leq \frac{p_D - R_2 - R_1}{2 \tan \theta} \\ \frac{\int_0^{\sqrt{R_2^2 - (x-p_D)^2}} \frac{p_D^2 + q^2 - R_2^2}{2p_D} I_{(x,y,z)} dx dy + \int_0^{\sqrt{q^2 - x^2}} \frac{\int_{p_D^2 + q^2 - R_2^2}^q I_{(x,y,z)} dx dy}{2p_D}}{2 \int_0^{\sqrt{q^2 - x^2}} \int_0^q I_{(x,y,z)} dx dy}, & \frac{p_D - R_2 - R_1}{2 \tan \theta} < z \leq \frac{p_D + R_2 - R_1}{2 \tan \theta} \\ \frac{\int_0^{\sqrt{R_2^2 - (x-p_D)^2}} \int_{p_D - R_2}^{p_D + R_2} I_{(x,y,z)} dx dy}{2 \int_0^{\sqrt{q^2 - x^2}} \int_0^q I_{(x,y,z)} dx dy}, & z > \frac{p_D + R_2 - R_1}{2 \tan \theta} \end{cases}, \quad (7)$$

where  $q = 2z \tan \theta + R_1$ .

#### 3.2 CTI Type

The cross-sectional front-end view and the plane geometry relationship are presented in Fig.5.



(a) front-end view (b) relationship between TF & RF

**Fig.5 Structure of the CTI type**

Set the middle TF as the thick fibre bundle with the parameters of core-radius  $R_1$  and the maximum divergence angle  $\theta$ . The core-radius of the RF is  $a_2$ . All

fibres have the same NA. The intensity-modulation function of the CTI type can be calculated as the combination of the P type made up by the middle TF bundle and any RF around.

Since the CTI type is closely combined by the TF bundle and all the receiving fibres, and the thickness of protection is much smaller than their core-radius, the axis distance between the TF bundle and the RF can be written as  $p_{CTI} = R_1 + a_2$ . Then the amount of the RF around is

$$N = \text{int}(\pi/a) = \text{int}[\pi/\arcsin(a_2/(R_1 + a_2))]$$

The intensity-modulation of the CTI type can be obtained as follows:

$$M_{CTI} = nM(R_1, a_2, \theta, p_{CTI}, z) = \begin{cases} 0, & z \leq \frac{p_{CTI} - a_2 - R_1}{2 \tan \theta} \\ n \cdot \frac{\int_0^{\sqrt{a_2^2 - (x - p_{CTI})^2}} \int_{p_{CTI} - a_2}^{\frac{(p_{CTI}^2 + q^2 - a_2^2)}{2p}} I(x, y, z) dx dy + \int_0^{\sqrt{q^2 - x^2}} \int_{\frac{(p_{CTI}^2 + q^2 - a_2^2)}{2p_{CTI}}}^q I(x, y, z) dx dy}{2 \int_0^{\sqrt{q^2 - x^2}} \int_0^q I(x, y, z) dx dy}, & \frac{p_{CTI} - a_2 - R_1}{2 \tan \theta} < z \leq \frac{p_{CTI} + a_2 - R_1}{2 \tan \theta} \\ n \cdot \frac{\int_0^{\sqrt{a_2^2 - (x - p_{CTI})^2}} \int_{p_{CTI} - a_2}^{p_{CTI} + a_2} I(x, y, z) dx dy}{2 \int_0^{\sqrt{q^2 - x^2}} \int_0^q I(x, y, z) dx dy}, & z > \frac{p_{CTI} + a_2 - R_1}{2 \tan \theta} \end{cases} \quad (8)$$

where  $q = 2z \tan \theta + R_1$ .

### 3.3 DC Type

As shown in Fig.6, the radius of the TF (bundle) is  $R_1$ , and those of the middle and the outer circles are  $R_2$  and  $R_3$ . The core-radius of all receiving fibres is  $a_2$ . Each fibre (bundle) has the same NA and the same maximum divergence angle  $\theta$ . Assume that the thickness of the protection for fibres is too thin to be calculated, then the axis distance between the TF (bundle) and the middle circle  $P_1 = R_1 + a_2$ , and the axis distance between the TF (bundle) and the outer circle  $p_2 = R_1 + 3a_2$ .

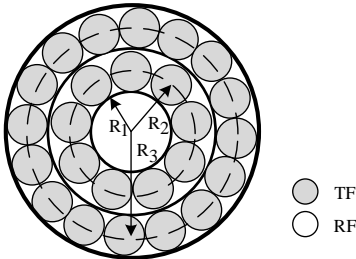


Fig.6 Structure of the DC type

The DC type can be equivalent to two sets of the CTI type working together. One is comprised by the TF (bundle) and the receiving fibres in the middle circle, and the other is constituted by the TF (bundle) and the receiving fibres in the outer circle. The intensity-modulation function of the first set is  $M_1$  and that of the second is  $M_2$ , so the intensity-modulation function of the DC type is expressed as

$$M_{DC} = \frac{M_2}{M_1} \quad (9)$$

The calculations of the intensity-modulation function  $M_1$  and  $M_2$  are similar to that in Section 3.2.

$$\begin{cases} M_1 = n_{r1} M(R_1, a_2, \theta, p_1, z) \\ M_2 = n_{r2} M(R_1, a_2, \theta, p_2, z) \end{cases} \quad (10)$$

$$\text{where } n_{r1} = \text{int} \left[ \frac{\pi}{\arcsin(\frac{a_2}{p_1})} \right], n_{r2} = \text{int} \left[ \frac{\pi}{\arcsin(\frac{a_2}{p_2})} \right]$$

Hence, the intensity-modulation function of the DC type can be written as

$$M_{DC} = \frac{M_2}{M_1} = \frac{n_{r2} M(R_1, a_2, \theta, p_2, z)}{n_{r1} M(R_1, a_2, \theta, p_1, z)} \quad (11)$$

### 3.4 R Type

The cross-sectional front-end view of the R type is presented in Fig.2(e). The R type OFBDS is consisted of  $n_t$  transmitting fibres and  $n_r$  receiving fibres, as shown in Fig.7. The radius of the whole bundle is  $R$ . Each fibre-core radius is  $a$ , and the maximum divergence angle is  $\theta$ . The working principle of the R type can be considered as  $n_t n_r$  sets of the P type randomly arranged with each other closely with the parameters  $a$  and  $\theta$  working together.

Set the intensity-modulation function of the P type combined by the  $i_{th}$  TF and the  $j_{th}$  RF as

$$M_{ij} = \frac{\Phi_{rij}}{\Phi_{ti}} \quad (12)$$

where  $\Phi_{ti}$  is the output light flux of the  $i_{th}$  TF and  $\Phi_{rij}$  is the received light flux of the  $j_{th}$  RF only from the  $i_{th}$  TF. With the same fibre parameters and light source, the output light flux of each TF in the R type is identical, that is  $\Phi_t = \Phi_{ti}$ , and the total output light flux  $Q_t = n_t \Phi_t$ .

The total received light flux of the R type OFBDS  $Q_r$  equals to the sum of  $\Phi_{rij}$  ( $j=1$  to  $n_r$ ,  $i=1$  to  $n_t$ ).

Therefore, the intensity-modulation function of the R type can be written as

$$M_R = \frac{Q_r}{Q_t} = \frac{\sum_{j=1}^{n_r} \sum_{i=1}^{n_t} \Phi_{rij}}{n_t \Phi_t} = \frac{\sum_{j=1}^{n_r} \sum_{i=1}^{n_t} M_{ij}}{n_t} \quad (13)$$

When  $M_{ij}=M(a_1, a_2, \theta, p_{ij}, z)=M(a, \theta, p_{ij}, z)$  in Eq. (13), the  $M_R$  calculation is equal to the calculation of any axis distance  $P_{ij}$  between any TF and RF in all  $n_t, n_r$  sets of the arranged P type OFBDS randomly.

According to Ref. [11], the calculation method for  $p_{ij}$  under rectangular coordinate system is

$$p_{ij} = (2a + 2c + g) \cdot$$

$$\sqrt{(x_i - x_j)^2 + (y_i - y_j)^2 + (x_i - x_j)(y_i - y_j)} \quad (14)$$

where  $a$  is the radius of the TF and the RF;  $c$  is the thickness of the protection for fibres; and  $g$  denotes the shortest distance between any two adjacent fibres. Meanwhile, the arrangement regulation of the TF and RF in the R type OFBDS is summarized as follows<sup>[11]</sup>:

$$\begin{cases} T(x, y) \in \{(x, y) \mid \text{mod}\left(x + \frac{3}{2}, \frac{3}{2}\right) = 0 \cap s \leq R - \frac{2r+2c+g}{2}\} \\ R(x, y) \in \{(x, y) \mid \text{mod}\left(x + \frac{3}{2}, \frac{3}{2}\right) \neq 0 \cap s \leq R - \frac{2r+2c+g}{2}\} \end{cases} \quad (15)$$

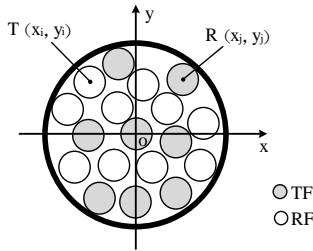


**Fig.7 Distribution of TF and RF under rectangular coordinate system**

### 3.5 H Type

The structure of the H type is given in Fig.2(f). Obviously, the H type OFBDS has the same amount of transmitting fibres and receiving fibres according to its structure characteristics, so  $n_t=n_r=n$ , the radius of each

fibre is  $a$ , and the NA and  $\theta$  are identical. The radius of the whole H type OFBDS is  $R$ . Parallel to the intensity-modulation function of the R type, the H type is similar with Eq. (14).

$$M_H = \frac{Q_r}{Q_t} = \frac{\sum_{j=1}^{n_r} \sum_{i=1}^{n_t} \Phi_{rij}}{n_t \Phi_t} = \frac{\sum_{j=1}^{n_r} \sum_{i=1}^{n_t} M(a, \theta, p_{ij}, z)}{n_t} \quad (16)$$

where  $p_{ij} = (2a + 2c + g)$

$$\sqrt{(x_i - x_j)^2 + (y_i - y_j)^2 + (x_i - x_j)(y_i - y_j)}$$

It was noticed that the distribution of TF and RF in the H type was different from that in the R type under rectangular coordinate system, which was also proposed in Ref. [11] as follows:

$$\begin{cases} T(x, y) \in \{(x, y) \mid x + \frac{y}{2} < 0 \cap s \leq R - \frac{2r+2c+g}{2}\} \\ R(x, y) \in \{(x, y) \mid x + \frac{y}{2} \geq 0 \cap s \leq R - \frac{2r+2c+g}{2}\} \end{cases} \quad (17)$$

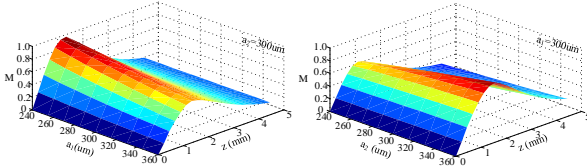
## 4 Simulation

### 4.1 Influence of Change of Fibre Core Radius on Intensity-Modulation Characteristics

When the other fibre parameters were unchanged and all fibres were closely arranged, the intensity-modulation characteristics of each type OFBDS analysed above were simulated to the influence caused by the change of fibre core-radius based on the Eqs. (6) (7) (8) (11) (13) (16). Set  $NA=0.22$ , the modulation coefficient  $\zeta=0.5$ <sup>[12]</sup>, and the  $z$ -axis coordinates in the figures below were normalized.

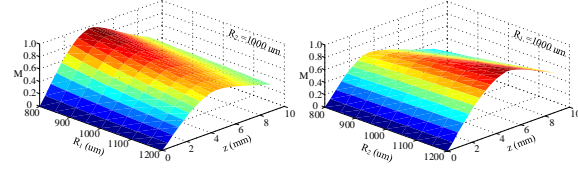
For the P type, the D type, the CTI type, and the DC type (in Figs.8-11), when the radius of TF (bundle) increased, the starting distance  $d_0$  remained, the peak distance  $[d_0, d_p]$  increased, the peak value  $M_p$  decreased, and the forward sloop displacement sensitivity  $S_f$  showed a decreasing trend with other conditions maintained unchanged. When the radius of the RF increased in the P type, the D type, and the CTI type, the starting distance  $d_0$  remained, while the peak distance  $[d_0, d_p]$ , the peak value  $M_p$ , and the forward sloop displacement sensitivity  $S_f$  increased. However, in the DC type structure,  $d_0$ ,  $[d_0, d_p]$ ,  $M_p$ , and  $S_f$  all increased with the increase of the radius of RF.

It can be seen from Fig.12 that  $d_0$  was almost zero,  $[d_0, d_p]$  increased,  $M_p$  had no significant change, and  $S_f$  decreased when the core-radius of TF and RF both changed.



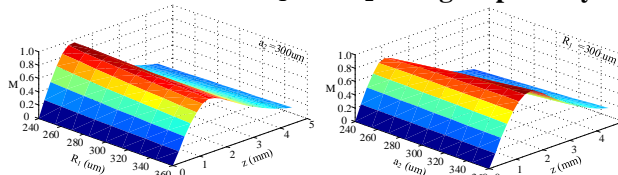
(Left: Changing the value of  $a_1$  and keep  $a_2$  constant;  
Right: Changing the value of  $a_2$  and keep  $a_1$  constant)

**Fig.8 Simulation of the P type intensity-modulation characteristics when  $a_1$  and  $a_2$  change separately**



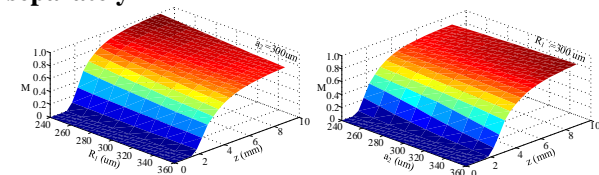
(Left: Changing the value of  $R_1$  and keep  $R_2$  constant;  
Right: Changing the value of  $R_2$  and keep  $R_1$  constant)

**Fig.9 Simulation of the D type intensity-modulation characteristics when  $R_1$  and  $R_2$  change separately**



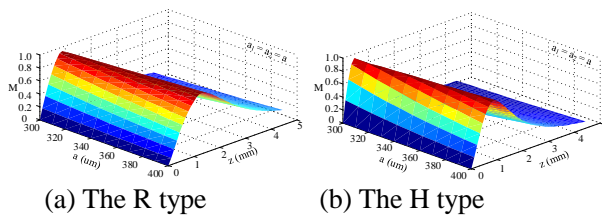
(Left: Changing the value of  $R_1$  and keep  $a_2$  constant;  
Right: Changing the value of  $a_2$  and keep  $R_1$  constant)

**Fig.10 Simulation of the CTI type intensity-modulation characteristics when  $R_1$  and  $R_2$  change separately**



(Left: Changing the value of  $R_1$  and keep  $a_2$  constant;  
Right: Changing the value of  $a_2$  and keep  $R_1$  constant)

**Fig.11 Simulation of the DC type intensity-modulation characteristics when  $R_1$  and  $a_2$  change separately**



(a) The R type

(b) The H type

**Fig.12 Simulation of the R type and the H type intensity-modulation characteristics when the core radii of TF and RF change together**

## 4.2 Influence of Change of NA on Intensity-Modulation Characteristics

The simulation requirement was the same with that in Section 5.1, and only the NA of each type was changed. The simulation curves of the intensity-modulation characteristics of each type are presented below. The  $M$  value in Fig.13 was normalized.

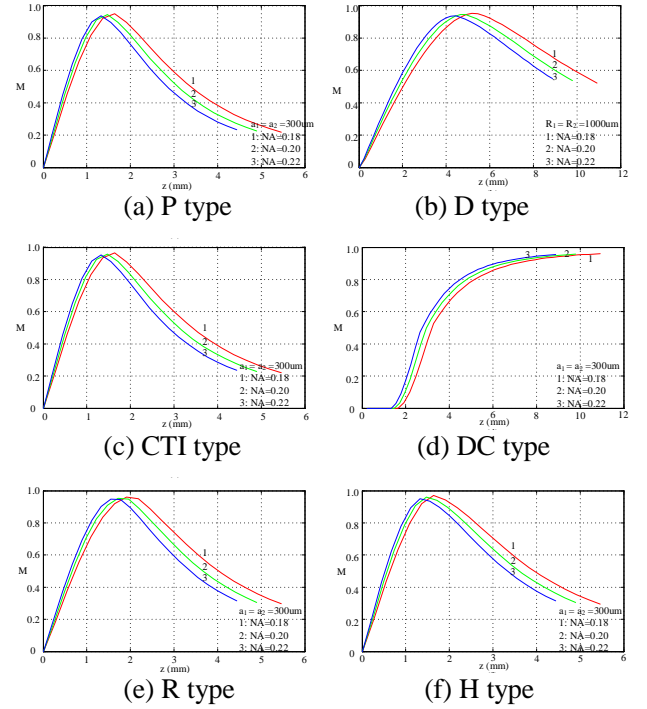


**Fig.13 Simulation of intensity-modulation characteristics when NA changes**

As illustrated above, when NA increased,  $[d_0, d_p]$  gradually reduced, and  $d_0$  and  $M_p$  were essentially constant with other conditions unchanged. Therefore, the linear range of the forward sloop became shorter and  $S_f$  increased. In particularly,  $d_0$  decreased when the NA of the fibres increased only in the DC type.

## 4.3 Influence of Change of Axis Distance between TF (Bundle) and RF (Bundle) on Intensity-Modulation Characteristics

When the radius and NA of each fibre were unchanged, the simulation of the influence of the change of the axis distance between TF (bundle) and RF (bundle) on intensity-modulation characteristics is



shown in Fig.14 according to Eqs. (6) (7) (8) (11) (13) (16).

It should be noticed that the R type and the H type had the structural feature of all fibres combined, thus

the analysis of the influence of the axis distance on them was not taken account of.

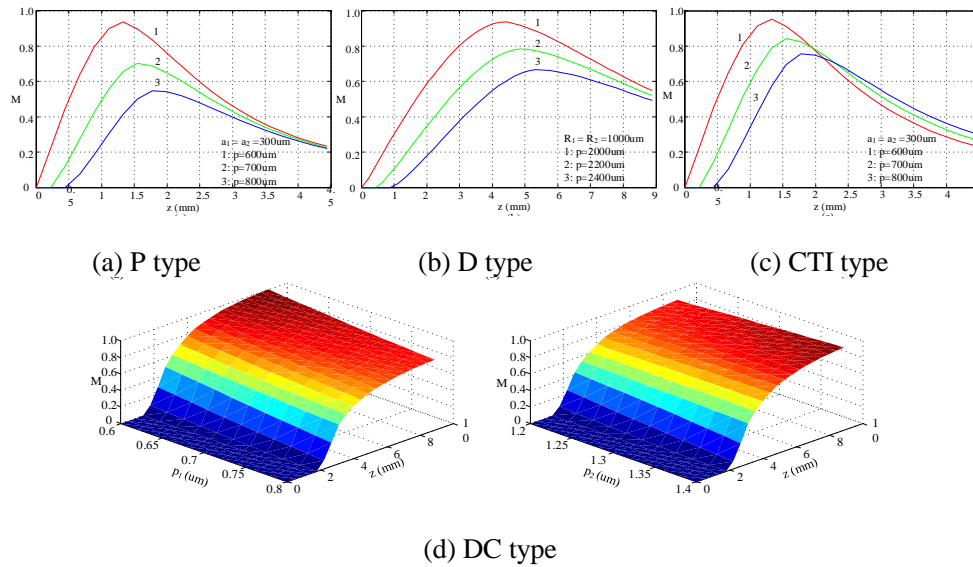


**Fig.14 Simulation of intensity-modulation characteristics when the axis distance changes**

The simulation results show that with the growth of the axis distance between TF (bundle) and RF (bundle),  $d_0$  and  $[d_0, d_p]$  increased while  $M_p$  and  $S_f$  reduced in the P type, the D type, and the CTI type. For the DC type structure, when only the axis distance between the TF (bundle) and the middle circle  $p_1$  increased,  $d_0$  enlarged while  $[d_0, d_p]$  and  $M_p$  reduced, and  $S_f$  remained constant. When only the axis distance between the TF (bundle) and the outer circle  $p_2$

increased,  $d_0$ ,  $[d_0, d_p]$ , and  $M_p$  all enlarged, and  $S_f$  also had an increasing trend.

#### 4.4 Selection of the Sensor Fibre Bundle Structure

Based on the above analysis, it can be seen that the CTI type fibre bundle had better light intensity modulation characteristics. Therefore, according to the simulation results, the designed fibre bundle parameters are presented in Table 1.

**Table 1 Design parameters of the sensor fiber probe**

Emitting fibre (EF)(one fibre)			Receiving fibres (RFs) (six fibres)			Fibre type	Diameter of middle fibre bundle ( $a$ )( $\mu\text{m}$ )
Fibre radius (nucleus)( $\mu\text{m}$ )	Fibre cladding ( $\mu\text{m}$ )	$NA$	Fibre radius (nucleus)( $\mu\text{m}$ )	Fibre cladding ( $\mu\text{m}$ )	$NA$		
150	15	0.22	150	15	0.37	Standard multimode optical fibre	1050

## 5 Design of Fibre Sensor System

### 5.1 Design of the Hardware System

#### 5.1.1 Light source

JW3105B box-type red source uses the Laser diode as light emitting device, and the laser drive circuit ensures that the laser has a constant power output. JW310B was used as the sensor light source.

#### 5.1.2 Design of photoelectric conversion circuit

Since the receiving light intensity of the optical fibre displacement sensor is very weak, the OPT101 (made by Burr-Brown Company) chip was chosen as the Photoelectric conversion Device, which has a large measurement area that collects a significant amount of light, and thus allows for high-sensitivity measurement. The internal feedback resistor was laser trimmed to 1 MΩ. Using this resistor, the output voltage responsivity (RV) was approximately 0.45 V/μw at 650 nm wavelength. Based on the diagram of OPT101 equivalent circuit as shown in Fig.15, the model of OPT101 is as follows:

$$H_1(s) = \frac{R_2 / \frac{1}{sC}}{R_1} = \frac{R_2}{R_1} \cdot \frac{1}{R_2 Cs + 1} \quad (18)$$

where  $R_1 = 10 \text{ k}\Omega$ ,  $R_2 = 1 \text{ M}\Omega$ , and  $C = 11 \text{ pF}$ .

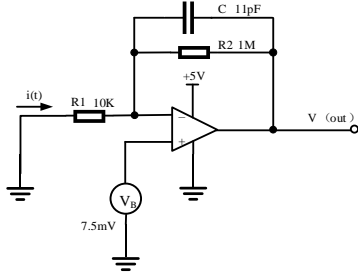


**Fig.15 Diagram of OPT101 equivalent circuit**

### 5.1.3 Signal amplifier module

Since the output voltage of OPT101 is in millivolt level, an AD620 was used as the core amplifier to enlarge the output voltage. AD620 is a commonly used single chip instrumentation amplifier, whose variable gain ranges up to 1000 and the extremely wide operating voltage ranges from  $\pm 2.3 \text{ V}$  to  $\pm 18 \text{ V}$ . The functional structure diagram of AD620 is shown in Fig.16.

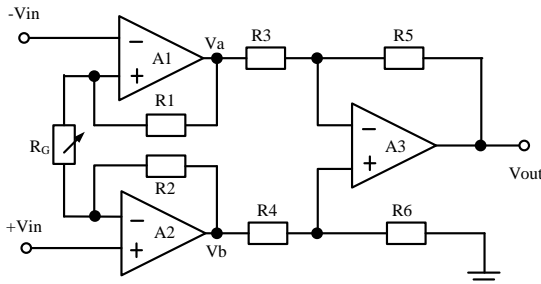


**Fig.16 Diagram of AD620 functional structure**

Based on the functional structure of AD620, the amplification calculated is

$$G = \frac{47.4}{R_G} + 1 \quad (19)$$

where  $G$  is the amplification of the circuit, and  $R_G$  (KΩ) is the external gain resistor.

### 5.1.4 Design of lowpass filter modules

Considering that the output voltage signal of the photoelectric conversion chip may be affected by the photoelectric tube noise and the circuit noise in the system, an active filter based on MAX274 monolithic integrated is designed in this paper. The schematic diagram of the filter circuit is shown in Fig.17.

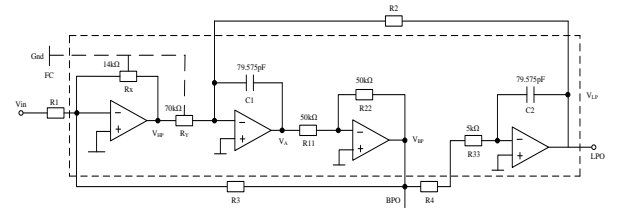


**Fig.17 Schematic diagram of filter circuit**

According to Fig.17, the transfer function of the filter can be calculated as

$$\begin{cases} \frac{V_{in}}{R_1} = -\frac{V_{BP}}{R_3} - \frac{V_{HP}}{R_X} \\ \frac{V_{HP}}{R_Y} = -\frac{V_A}{1/sC_1} - \frac{V_{LP}}{R_2} \\ \frac{V_A}{R_{11}} = -\frac{V_{BP}}{R_{22}} \\ \frac{V_{BP}}{R_4 + R_{33}} = -\frac{V_{LP}}{1/sC_2} \end{cases} \quad (20)$$

$$H_2(s) = \frac{V_{LP}}{V_{IN}} = \frac{\frac{R_X}{R_Y R_1 C_1 C_2 (R_4 + R_{33})}}{s^2 + s \frac{R_X}{R_Y R_3 C_1} + \frac{1}{C_1 C_2 R_2 (R_4 + R_{33})}} \quad (21)$$

The typical expression for the filter transfer functions is

$$A(s) = \frac{A_0 \frac{s}{Q\omega_0}}{1 + \frac{s}{Q\omega_0} + \left(\frac{s}{\omega_0}\right)^2} \quad (22)$$

Based on formulae (21) and (22), the centre frequency of the lowpass filter  $\omega_0$ , the Quality factor  $Q$ , and the system gain  $G$  can be obtained as follows:

$$\omega_0 = \sqrt{\frac{1}{R_2 C_1 C_2 (R_4 + R_{33})}} \quad (23)$$

$$Q = \sqrt{\frac{1}{R_2 C_1 C_2 (R_4 + R_{33})}} \frac{R_Y}{R_X} R_3 \quad (24)$$

$$G = \frac{R_3}{R_1} \quad (25)$$

According to formulae (23)-(25), the mathematical relationship between  $R_1$ ,  $R_2$ ,  $R_3$ , and  $R_4$  can be obtained as

$$\begin{cases} R_1 = \frac{R_3}{G} \\ R_2 = \frac{2 \times 10^9}{F_0} \\ R_3 = \frac{Q \times 2 \times 10^9}{F_0} \times \frac{R_x}{R_y} \\ R_4 = R_2 - 5k\Omega \end{cases} \quad (26)$$

Considering the maximum output bandwidth of the OPT101 is 23 kHz, so 23 kHz was designed as the sensor bandwidth. For formula (26),  $R_1=16 \text{ k}\Omega$ ,  $R_2=46 \text{ k}\Omega$ ,  $R_3=16 \text{ k}\Omega$ , and  $R_4=46 \text{ k}\Omega$  were selected for the design.

## 5.2 Sensor Measurement Equations

The sensor measurement equation can be written as

$$V = 6GR_f S_p P \quad (27)$$

where  $G$  is the amplification calculated by formula (19);  $R_f$  is the internal load resistance of the photoelectric;  $S_p$  is the sensitivity of the OPT101 calculated by formula (18); and  $P$  is the receiving light intensity of single fibre.

According to formulae (1) and (27),

$$V = 6GR_f S_p P = 6GR_f S_p \cdot \iint_S \frac{K_0 I_0}{\pi a^2 [1 + \zeta(z/a)^{3/2} \tan \theta]^2} \cdot \exp\left\{-\frac{r^2}{a^2 [1 + \zeta(z/a)^{3/2} \tan \theta]^2}\right\} ds \quad (28)$$

where  $K_0$  is the loss rate of the fibre sensor.

Since the size of the fibre end surface is small, the light intensity at the centre of the receiving face can be used as the average light intensity of each receiving fibre surface, then the simplified sensor measurement formula can be written as

$$V = 6GR_f S_p \cdot \frac{SK_0 I_0}{a^2 [1 + \zeta(z/a)^{3/2} \tan \theta]^2} \quad (29)$$

where  $S$  is the receiving area of the single fibre. Combined with the fibre bundle design parameters in Table 1, the output character of the CTI type sensor is shown in Fig.18.

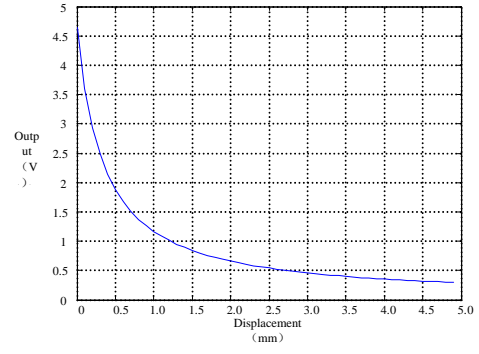


Fig.18 Simulation result of the sensor output

## 6 Experiment and Results

### 6.1 Static Measurement Test

#### 6.1.1 Calibration

The helical micro-measuring device was used for the sensor calibration. In the experiment, a plane was pushed to move in the axis direction of the fibre sensor probe. The plane was moved away from 0 to 6 mm before the sensor surface with a step of 0.1 mm. The process and return curve of the sensor are shown in Fig.19. The process and return calibration experiment were conducted for ten times, and the curve was fitted using the least square method. It can be seen from Fig.19 that the sensor had a measurement range of about 3 mm, and the calibration results curve was very similar with the simulation result in Fig.18.

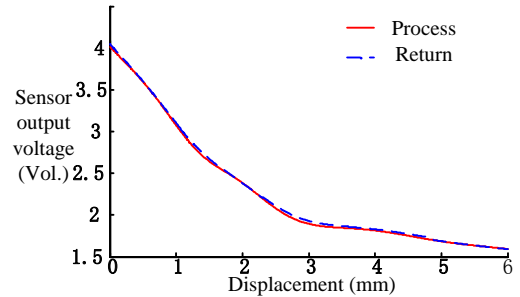
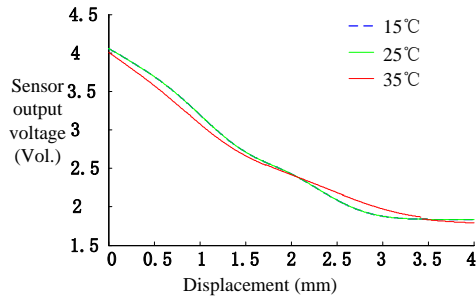


Fig.19 Calibration results of the fibre sensor

#### 6.1.2 Temperature interference experiment

The room temperature was set at 15°C, 25°C, and 35°C, and the output measurement of the sensor at different temperatures was achieved. After repeated measurements, the average value of each set of data at different temperatures was obtained. The least squares fitting results of them are shown in Fig.20.



**Fig.20 Fibre sensor output at different temperatures**

From Fig.20, it can be seen that the output of the sensor system slightly fell in the measurement range of 0~2 mm with the increase of the temperature. Temperature change had certain influence on the measurement result in this experiment. In order to ensure the measurement accuracy, the working environment temperature of photoelectric conversion and amplification filter circuit should be controlled in practical applications.

#### 6.1.3 Changes of the measured surface area of the plane

The possible effect of the changes of the measured plane area size on the measurement results was investigated. Four iron sheets with smooth surface were selected as the measurement plane. The iron sheets with different diameters and covered with mirror reflective film are presented in Fig.21. The measurement experiment was performed as described in Section 6.1.1, and the results are illustrated in Fig.22.

It can be seen that for different measurement plane areas with the same surface shader, the measured plane size had very little effect on the sensor output character.

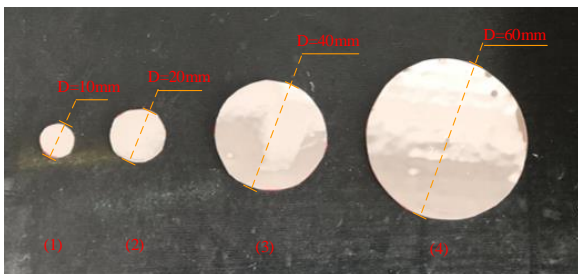


**Fig.21 Measured plane with different diameters**

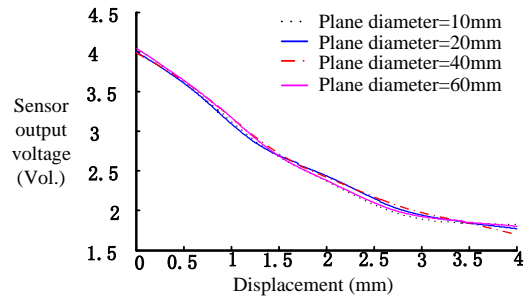


**Fig.22 Measurement results of the plane with different diameters**

## 6.2 Dynamic Measurement

The dynamic measurement experiments were realized on a rotor dynamic test platform as presented in Fig.23. The sensor probe and the rotor blade tip plane were kept with a distance, and the rotor rotation speed and the frequency of the blade passing before the sensor probe were changed at the same time. The rotor speed was changed to 1000 r/min, 2000 r/min, and 3000 r/min respectively, and the measurement results are shown in Fig.24.

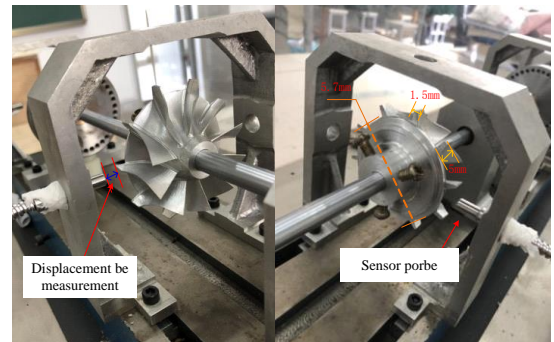


**Fig.23 Platform of the dynamic experiment**

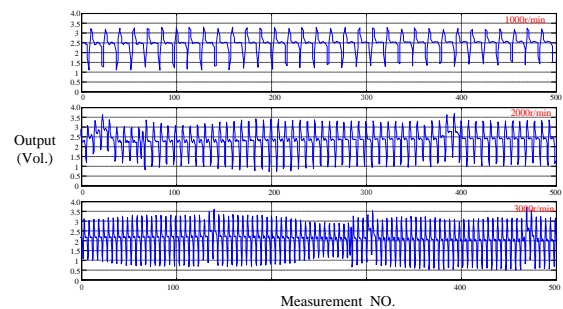


**Fig.24 Fibre sensor output at different rotor RPM**

The frequencies of the blade passing before the sensor were 0.17 kHz, 0.22 kHz, and 0.50 kHz. Based on sampling principle, the sample frequency was twice of the blade rotation speed at least to realize the information with no lost. It can be seen that the fibre

sensor can achieve the displacement between the blade tip surface and the probe surface completely, as shown in Fig.24.

## 7 Conclusions

The model of multi-structural OFBDS is presented in this paper. Based on the model, influences of the fibre core-radius, the NA, and the axis distance on intensity-modulation characteristic were analysed. Through the light intensity modulation character of different fibre bundle structures under the unified model comparison and analysis, the structure of the fibre displacement sensor probe was selected. Then, the sensor measurement equation and sensor hardware system were designed. In order to test the characteristic of the sensor, static experiment and dynamic experiment were conducted. Results showed that the transducer had excellent static and dynamic characteristics.

## References

- [1] Buchoud E, Vrabie V, Mars J I, et al. Quantification of submillimeter displacements by distributed optical fiber sensors. *IEEE Transactions on Instrumentation & Measurement*, 2016, 65(2): 413-422. DOI: 10.1109/TIM.2015.2485340.
- [2] Chetia D, Basumatary T, Singh H K, et al. Low-cost refractometer with longitudinally displaced optical fibers. *IEEE Sensors Journal*, 2016, 16(15): 5950-5957. DOI: 10.1109/JSEN.2016.2576779.
- [3] Su J, Dong X, Lu C. Property of bent few-mode fiber and its application in displacement sensor. *IEEE Photonics Technology Letters*, 2016, 28(13): 1387-1390. DOI: 10.1109/LPT.2016.2542366.
- [4] Kim H H, Choi S J, Yi H, et al. Novel non-contact optical fiber displacement sensor using bidirectional modulation of a Mach-Zehnder electro-optical modulator. *Proceedings of 2014 OptoElectronics and Communication Conference and Australian Conference on Optical Fibre Technology*. Piscataway: IEEE, 2014. 847-849.
- [5] Wanninayake I B, Dasgupta P, Seneviratne L D, et al. Modeling and optimizing output characteristics of intensity modulated optical fiber-based displacement sensors. *IEEE Transactions on Instrumentation & Measurement*, 2015, 64(3): 758-767. DOI: 10.1109/TIM.2014.2347694.
- [6] Puangmali P, Althoefer K, Seneviratne L D. Mathematical modeling of intensity-modulated bent-tip optical fiber displacement sensors. *IEEE Transactions on Instrumentation & Measurement*, 2010, 59(2): 283-291. DOI: 10.1109/TIM.2009.2023147.
- [7] Jia B, He L, Yan G, et al. A differential reflective intensity optical fiber angular displacement sensor. *Sensors*, 2016, 16(9). DOI: 10.3390/s16091508.
- [8] Marzban M, Packirisamy M, Dargahi J. Fiber-mirror integrated compliant mechanical system for measuring force and displacement simultaneously. *Proceedings of 2015 Photonics North*. Piscataway: IEEE, 2015: 1-8. DOI: 10.1109/PN.2015.7292534.
- [9] Xie S, Zhang X. Design and modeling of three-dimensional tip-clearance optical probe based on two-circle reflective coaxial fiber bundle. *Proceedings of 2016 IEEE Sensors*, Piscataway: IEEE. DOI: 10.1109/ICSENS.2016.7808641.
- [10] Yuan Libo. Light source and the optical field formed by an optical fiber end. *Optical Communication Technology*, 1994, 18(1): 54-64. DOI: 10.13921/j.cnki.issn1002-5561.1994.01.012. (in Chinese)
- [11] Cao H, Chen Y, Zhou Z, et al. Theoretical and experimental study on the optical fiber bundle displacement sensors. *Sensors and Actuators A: Physical*, 2007, 136(2):580-587. DOI: 10.1016/j.sna.2006.12.010.
- [12] Jia B, He L. An optical fiber measurement system for blade tip clearance of engine. *International Journal of Aerospace Engineering*, 2017(5): 1-9. DOI: 10.1155/2017/4168150.